JOURNAL OF SPACECRAFT AND ROCKETS
Vol. 36, No. 2, March–April 1999

Heating Analysis of the Nosecap and Leading Edges of the X-34 Vehicle

Grant Palmer*
NASA Ames Research Center, Moffett Field, California 94035
and
Susan Polsky*
Thermosciences Institute, Sunnyvale, California 94087

Temperature, pressure, and heating rates were computed on the surface of the X-34 vehicle at six points along the X1004701 Mach 8.5 trajectory. The work focused on the nosecap, the wing/strake leading edges, and the rudder leading edge. These areas are protected from the thermal environments experienced during flight by silicone impregnated reusable ceramic ablator tiles. The computational data provided anchor points from which a time history of surface heating and pressure could be generated. This time history will be used to analyze and design the tiles. The Navier–Stokes solutions were compared with experimental data and engineering correlations. Bow-shock wave impingement on the wing leading edge was investigated. The location of impingement was a function of freestream Mach number and vehicle angle of attack. There was no bow-shock wave impingement seen on the rudder leading edge. A detailed grid sensitivity study was undertaken to establish an acceptable level of grid independence of the computed solutions.

Nomenclature

D = diffusion coefficient, m^2/s
h = specific enthalpy, J/kg
q = heat flux, W/m^2
r = radius, m
T = temperature, K
V = velocity, m/s
Z = bifurcation mass fraction
ε = emissivity
η = direction normal to vehicle surface
κ = thermal conductivity of gas, W/(m-K)
μ = viscosity, kg/(m-s)
ρ = density, kg/m^3
σ = Stefan–Boltzmann constant, $5.667e{-}8$ W/(m^2-K^4)

Subscripts

cond = conductive
e = boundary-layer edge
n = nose
s = species
t = total
w = wall
∞ = freestream

Introduction

THE X-34 vehicle will provide the first flight demonstation under NASA's reusable launch vehicle (RLV) program of a fully reusable launch vehicle. Under a fixed-price contract with NASA, Orbital Sciences Corporation (OSC) is to provide a Mach 8 suborbital RLV technology demonstrator. The vehicle is 18.3 m in length, has a wingspan of 8.4 m, and is powered by a single liquid oxygen–kerosene engine. The X-34 vehicle is carried below an L-1011 aircraft to an altitude in excess of 9 km, where the vehicles separate, the X-34 engine starts, and the X-34 vehicle continues along its flight trajectory. The first flight is currently scheduled for 1999.

Under a cooperative agreement with OSC, NASA Ames Research Center was given the responsibility to design, analyze, and fabricate the thermal protection system (TPS) of the X-34 vehicle nosecap, wing leading edges, and rudder leading edge. The surface of the X-34 vehicle with the nosecap and leading edges highlighted is shown in Fig. 1. These surfaces will be protected from the thermal environments experienced during flight by silicone impregnated reusable ceramic ablator (SIRCA) tiles. The material is a ceramic/organic composite consisting of a fibrous silica substrate with a silicone impregnant. SIRCA tiles have a low material density and thermal conductivity, are resistant to water absorbtion, exhibit high strain to failure characteristics, and can withstand heat fluxes up to 200 W/cm^2.

The purpose of this paper is to compute computational fluid dynamic (CFD) flow solutions at six points along the baseline Mach 8 trajectory with the emphasis on the nosecap, wing leading edge, and rudder leading edge. A complimentary effort was undertaken at NASA Langley Research Center to provide acreage heating data for the blanket TPS design.[1–4] The solutions presented in this work served as anchor points from which a time history of pressure and heating rate on the surfaces of the nosecap, wing leading edges, and rudder leading edge can be generated. The time histories of pressure and heating rate are used by the tile designers to verify the thermal and structural integrity of the tile design. The CFD solutions also can be used to analyze the presence and impact of bow-shock wave impingement on the wing and rudder leading edges.

Methodology

The surface and volume grids used by the three-dimensional Navier–Stokes flow solver were generated from Initial Graphics Exchange Specification geometry data using the GRIDGEN[5] grid generator. Three different volume grids were used to reduce the individual problem size and improve solution throughput on the NASA Cray C-90 computers. Grid 1 was a 65-point streamwise, 65-point circumferential, and 65-point normal nosecap grid extending 0.54 m aft of the nose. Grid 2 was a 169-point streamwise, 129-point circumferential, and 65-point normal wing/strake grid extending from the nose to the wing-tip trailing edge. This grid included an 89 × 33 × 65 region to characterize the wing/strake leading edge but did not include the rudder and had far less resolution of the nosecap region than did grid 1. Grid 3 was a 117-point streamwise, 93-point circumferential, and 65-point normal grid extending from the nose to the tail-root trailing edge. This grid included a 17 × 13 × 65 zone that modeled the rudder leading edge but had less resolution of the

---

Received Feb. 12, 1998; revision received July 13, 1998; accepted for publication Aug. 1, 1998.

*Research Scientist. Senior Member AIAA.

wing leading edge than did grid 2. In this case only half of the rudder leading edge was modeled because of vehicle symmetry. Each of the grids used a hyperbolic tangent distribution of normal points with a first grid spacing normal to the wall of 1.0e−6 m. A 1-μ spacing was felt to be more than adequate to properly resolve the boundary layer along the entire flight trajectory.

The flow solutions were computed using the General Aerodynamic Simulation Program (GASP) version 3 Navier–Stokes flow solver.[6] GASP is an established commercial code that has been applied to a wide array of internal and external flow problems.[7–11] Solutions using GASP have been validated against Space Shuttle flight data.[7,8] GASP solves the full Navier–Stokes equations that model the conservation of density, momentum, and energy. Third-order spatially accurate Van Leer flux vector splitting[6] is used to difference the inviscid fluxes. Viscous terms are evaluated in all three coordinate directions.

A five-species, finite-rate reacting gas air chemistry model is used for all computations to resolve any real gas effects that may exist. The reaction rate model is that of Park.[12] The species specific heats and enthalpies are obtained by assuming the internal energy modes are in translational, rotational, and vibrational equilibrium. Species viscosity is obtained using Blottner curve fits.[13] Mixture laminar viscosity is computed using Wilke's mixing rule.[14] Species thermal conductivity is calculated using Eucken's relation.[15] Mixture thermal conductivity is obtained using Wilke's mixing rule. Species diffusion is assumed to be binary. The diffusion coefficients are obtained by assuming a constant Schmidt number. All turbulent flow solutions used the Baldwin–Lomax turbulence model.[16]

The surface temperature is computed by solving an energy balance at the vehicle surface[9]:

$$\kappa\frac{\partial T}{\partial \eta} + \sum_{s=1}^{\mathrm{nspc}} \rho D h_s \frac{\partial Z_s}{\partial \eta} = \sigma \varepsilon T_w^4 + q_{\mathrm{cond}} \qquad (1)$$

For the calculations presented in this study, a constant emissivity of 0.85 was applied to the entire vehicle. The emissivity of charred SIRCA is a weak function of temperature and varies between 0.85 and 0.90. The rest of the X-34 vehicle TPS consists of blanket insulation that has a lower emissivity. Because the emphasis of this study was the SIRCA tile surfaces, the 0.85 value was applied over the entire surface. Conduction into the vehicle surface was not modeled, and so the q_{cond} term was set to zero. This assumption is reasonable for ceramic TPS materials with low thermal conductivities.

The CFD results in this paper are compared with both experimental and analytical data. The experimental comparisons are discussed in the next section. It is possible to compare the CFD value of heating rate on the nosecap with an engineering correlation that provides laminar stagnation point heat transfer to a sphere[17]:

$$q = 1.83 \times 10^{-8}\sqrt{(\rho_\infty / r_n)}\,V_\infty^3[1 - (h_w/h_t)]\ \mathrm{W/cm^2} \qquad (2)$$

The X-34 vehicle nosecap is spherical with a nose radius of 0.179 m. The preceding relation is applicable for the angle-of-attack range the X-34 vehicle will experience.

Comparison with Experiment

A 0.0183-scale model of the X-34 vehicle was tested in the NASA Langley Research Center 20-Inch Mach 6 tunnel. The model was fabricated using a phosphor-coated ceramic that fluoresces in two regions of the visible spectrum when illuminated with ultraviolet light.[1] The fluorescence intensity is a function of the incident ultraviolet light and the surface temperature of the phosphors. The surface temperature on the model surface can be computed from color video images taken during the test.

A CFD calculation was performed at the experimental conditions. These conditions were Mach 6, 15-deg-angle-of-attack flow at a freestream temperature and density of 62.4 K and 0.1136 kg/m^3. Computations were performed both fully laminar and fully turbulent using a constant temperature wall-boundary condition of 300 K. The wing/strake grid, scaled to the proper model size, was used for the CFD computations. This grid had more surface grid resolution than the rudder grid but extended only to the trailing edge of the wing.

Figure 2a compares the experimental and computational heat transfer coefficients down the windward centerline and at two axial locations. The coefficients are normalized by the Fay–Ridell stagnation point heat transfer coefficient to a sphere.[18] The flow is laminar over the front part of the model and begins to transition to turbulent flow at an x/L value of about 0.3. The CFD matched the laminar heating along the windward centerline very closely. The CFD overpredicted the turbulent heating. The maximum difference between the CFD and experimental turbulent heating values is slightly more than the experimental uncertainty of 10%.

Figures 2b and 2c show the experimental and CFD heating coefficient results at two axial locations: $x/L = 0.2$, where the flow is laminar, and $x/L = 0.79$, where the flow is turbulent. In both cases the CFD does a good job of reproducing the experimental data. The laminar computation is largely within the experimental uncertainty of the measured results. The CFD turbulent data overpredict the heating near the centerline and underpredict the heating near the wing tip but are generally close to the experimental values.

Results

CFD Computation Points

Six points were analyzed on the X1004701 Mach 8.5 trajectory: time, altitude, Mach number, and angle of attack for these points are shown in Table 1. The first two points are during the vehicle ascent; the remaining four are during the vehicle descent. The 152-s point is close to the peak heating point on ascent. The 221-s point is the peak-Mach-number, peak-altitude point. The 324-s point is close to the peak heating point on descent. The 358-s point represents a high-heating-rate, low-angle-of-attack condition. The 294- and 600-s points were selected to add more definition to the time history heating rate profile. The freestream Reynolds number per unit length varied from 3455 at the 221-s point to 1.438e+6 at the 600-s point.

Turbulent Transition

The wing and rudder leading-edge computations assumed turbulent flow except at the 221-s trajectory point. At 221 s the vehicle is at an altitude of 80 km, where laminar flow over the nosecap and leading edges can be safely assumed based on the freestream

Table 1 CFD computation point values

Time, s	Altitude, km	Mach number	Angle of attack, deg
152	60.0	7.87	10.2
221	80.0	8.81	10.2
294	57.9	7.63	30.0
324	42.8	6.94	30.0
358	39.5	6.30	11.4
600	30.9	4.44	7.6

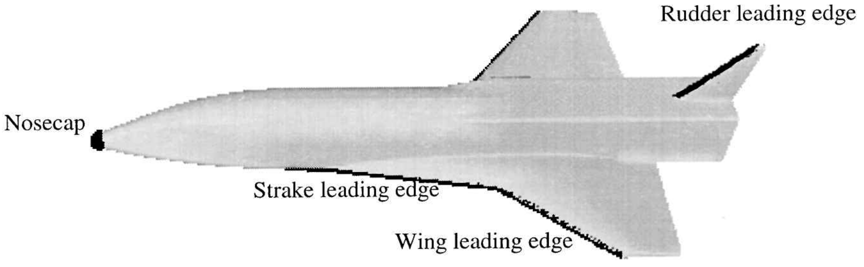

Fig. 1 X-34 vehicle surface geometry.

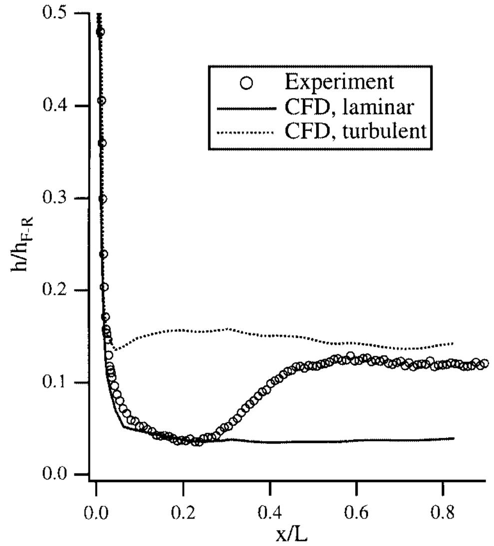

a) Windward centerline

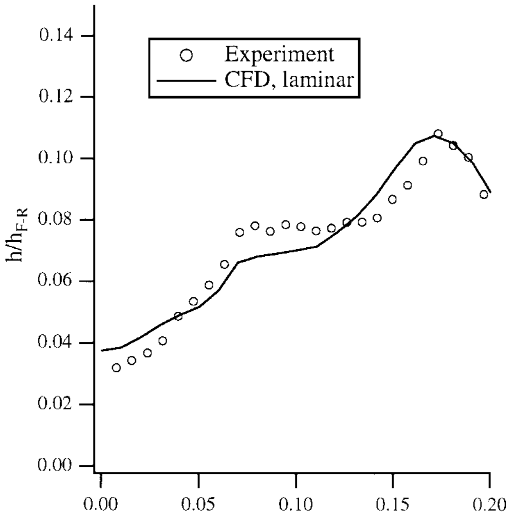

b) Laminar heating rate at *x*/*L* =0.2

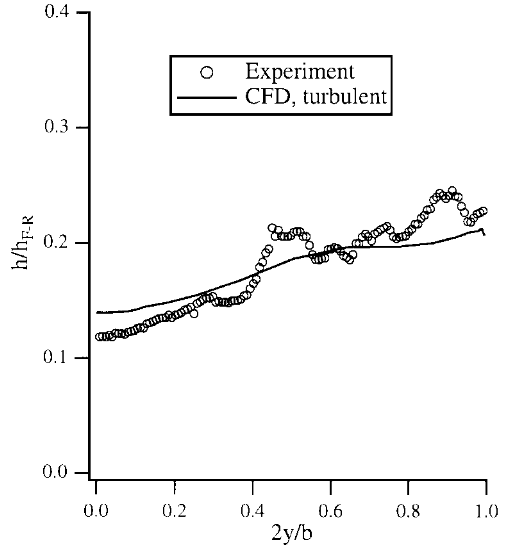

c) Turbulent heating rate at *x*/*L* = 0.79

Fig. 2 Comparison of experimental and computed surface heating rates.

density and Reynolds number. There is some question as to whether the flow over the nosecap would remain laminar at all six CFD computation points. At higher altitudes the flow over the nosecap would be laminar. At some point during the descent, the nosecap flow will transition and become turbulent.

In an attempt to assess the nature of the flow over the nosecap for the six CFD computation points, the following prediction correlation was applied to the X-34 vehicle[19]:

$$x_T = \frac{Re_T \mu_e}{\rho_e V_e} \tag{3}$$

The quantity x_T is the location of turbulent transition. The transition Reynolds number Re_T is obtained from the expression[19]

$$\log_{10}(Re_T) = 6.421 \exp\left(1.209 \times 10^{-4} M_e^{2.641}\right) \tag{4}$$

This correlation was based on Mach 10 cone data and has been used in a study of hypersonic waveriders.[20] When applied to the X-34 model at the Mach 6 experimental conditions described earlier, the correlation predicts a transition location of 0.12 m. The experimental transition location is approximately 0.11 m.

The most likely trajectory point for turbulent flow on the nosecap of the six CFD computation points is the 600-s point, where the vehicle is at 39-km altitude traveling at Mach 4.4. At these conditions the transition correlation predicts a transition location of 2.0 m. The back edge of the nosecap is 0.39 m aft of the nose. The flow over the nosecap can therefore be assumed to be laminar at all six CFD computation points.

Nosecap

The first local environment studied was the nosecap. Flow solutions were computed using grid 1. Computed heating rate profiles at the six CFD trajectory points are shown in Fig. 3a. Also shown in Fig. 3a are laminar stagnation point heating rate values on a sphere from Eq. (2). The Eq. (2) data points were placed at the stagnation point computed by the CFD. This location was a function of angle of attack and varied between the six computations. The peak surface heating rate occurs at the 324-s point and is 13.8 W/cm^2. This heating rate corresponds to a radiative equilibrium wall temperature of 1300 K. The CFD and engineering correlation stagnation heating rate values compare closely except at the 600-s point.

The peak value of total integrated heat load occurred at 0.0345 m from the nose and is 3660 J/cm^2. The total heat load drops off sharply from the peak value. At a distance of 0.25 m from the nose, the total integrated heat load is 1727 J/cm^2. At the back edge of the nosecap ($s = 0.393$ m), the total integrated heat load has dropped to 821 J/cm^2.

Figure 3b shows surface pressure values along the nosecap windward centerline. The peak computed value of 27,340 Pa occurs at the 600-s trajectory point where the freestream pressure is the highest. The six CFD points selected do not cover the entire dynamic pressure range. Peak dynamic pressures typically occur early in the ascent or late in the descent. Therefore, the peak surface pressure on the X-34 nosecap was not captured by the six CFD solutions performed.

Wing/Strake Leading Edge

The second area of the vehicle to be studied is the wing/strake leading edge. CFD solutions were run over grid 2 at the six trajectory points discussed previously. The flow was assumed to be fully turbulent flow over the entire length of the vehicle except at the 221-s point where the flow was assumed laminar due to the high altitude and low freestream Reynolds number. The maximum surface heating rate along the wing/strake leading edge is shown in Fig. 4a. The data shown on these curves are the maximum for each streamwise plane along the wing leading edge. The location of the maximum temperature and heating along each grid plane is a function of angle of attack and varies from trajectory point to trajectory point.

The trends of the CFD profiles are similar to those seen with the nosecap solutions. The peak surface heating rate on the wing leading edge occurs at the 324-s trajectory point and is 17.4 W/cm^2. This corresponds to a radiative equilibrium wall temperature of 1378 K. The

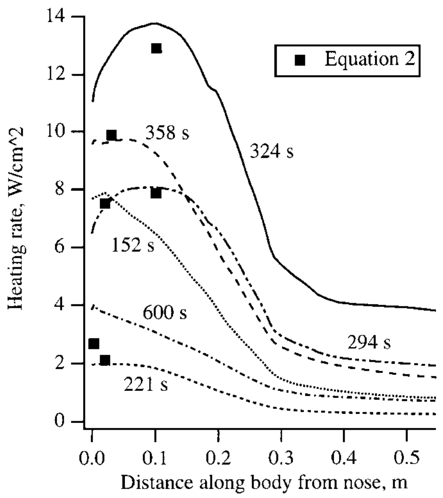

a) Surface heating rate

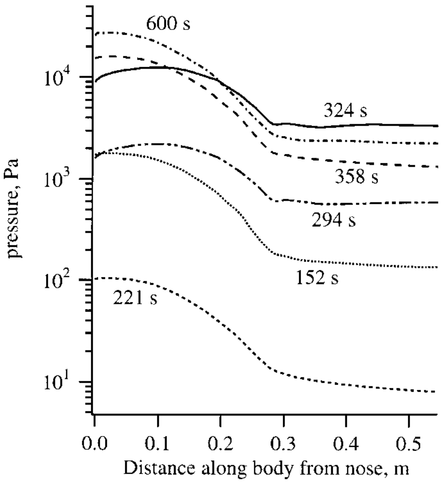

b) Surface pressure

Fig. 3 Nosecap windward centerline surface values.

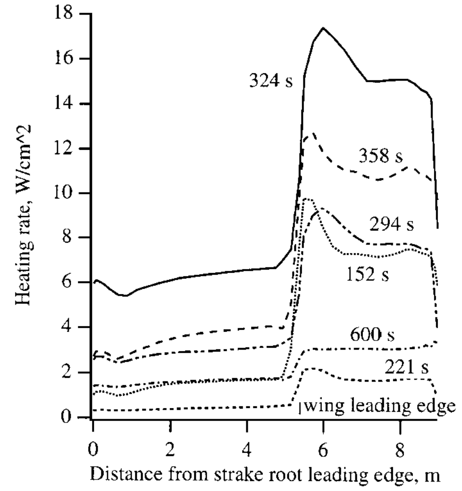

a) Surface heating rate

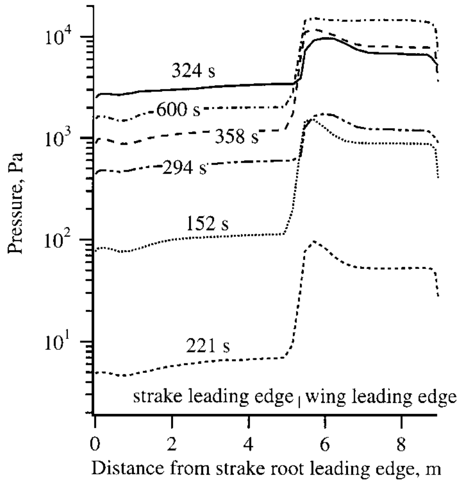

b) Surface pressure

Fig. 4 Wing/strake leading-edge surface values.

peak surface heating rate on the strake leading edge is 7.0 W/cm^2, corresponding to a temperature of 1098 K. The spike in the surface heating rate profiles is due to bow-shock wave impingement on the wing leading edge and will be discussed in a subsequent section. The maximum total integrated heat load is 4669 J/cm^2 on the wing leading edge and 1565 J/cm^2 on the strake leading edge.

Figure 4b shows surface pressure profiles. The maximum surface pressure on the wing leading edge occurs at the 600-s trajectory point and is 15,090 Pa. The maximum surface pressure on the strake leading edge occurs at the 324-s trajectory point and is 3401 Pa. The strake leading-edge maximum occurred at the 324-s point because the strake leading edge is enclosed by the bow-shock wave and is more influenced by that than it is by the freestream density magnitude.

Rudder Leading Edge

The third local vehicle environment studied was the rudder leading edge. Solutions were computed at the six CFD trajectory points using grid 3. The surface profiles along the rudder leading edge are shown in Fig. 5a. Unlike the nosecap and wing/strake leading-edge solutions, the peak surface heating rate on the rudder leading edge does not occur at the 324-s point, but instead the peak values are seen at the 358-s point. At the 294- and 324-s trajectory points, the vehicle is at an angle of attack of 30 deg. The fuselage shields the rudder from the flow, and the heating is relatively low. At the 358-s trajectory point the vehicle has pitched down to an angle of attack of 11.4 deg, and more of the rudder is exposed to the flow. The peak heating rate along the rudder leading edge is 7.4 W/cm^2 and occurs near the rudder tip. The peak total integrated heat load is 2374 J/cm^2. The maximum value of leading-edge surface pressure, shown in Fig. 5b, is 3839 Pa and occurs at the 600-s trajectory point.

Bow-Shock Wave Impingement

One important design consideration is whether and where the bow-shock wave impinges on the wing/strake and rudder leading edge. To qualitatively investigate the location of the bow-shock impingement, temperature contours were plotted on the same geometric plane as the wing/strake leading edge, shown in Fig. 6. In each of the six trajectory points investigated, the bow-shock wave seems to impinge on the wing/strake leading edge. The location of the impingement is a function of Mach number and angle of attack. The impingement point is close to the wing/strake junction at the 152- and 221-s points but then moves further outboard at the 294- and 324-s points, where the vehicle has pitched up to an angle of attack of 30 deg. The impingement moves inboard when the vehicle pitches down to an angle of attack of 11.4 deg at the 358-s point. At the 600-s point, where the Mach number has decreased to 4.4, the impingement point is near the wing tip.

These results are only qualitative in nature. The main objective of this study was to compute surface heating rate and pressure, and the grids were designed to resolve those features. A detailed investigation of bow-shock wave impingement would involve increasing the spatial resolution in the shock region and a more rigorous criteria for locating the bow shock in the CFD solution. Still, the effects of the bow-shock wave impingement can be seen in the spikes observed in the heating-rate profiles from Fig. 4a.

The bow-shock wave was not found to impinge on the vertical tail at any of the trajectory points studied. The tail is relatively short

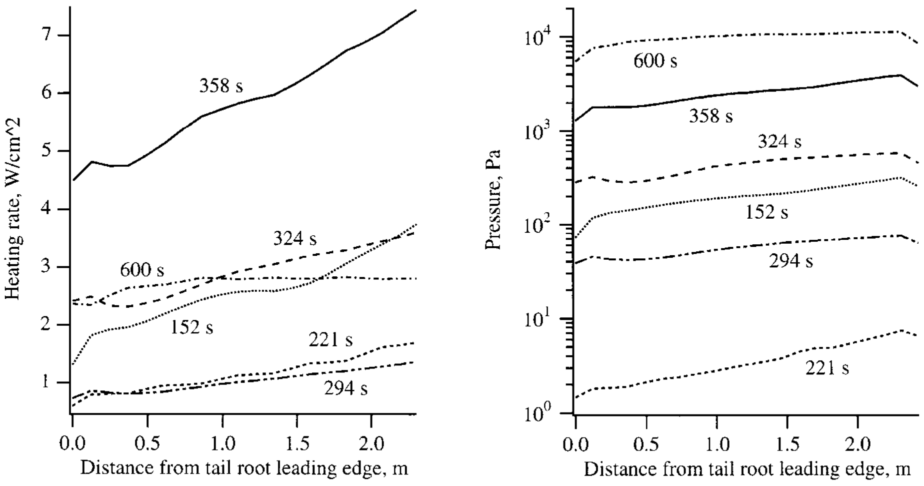

a) Surface heating rate **b) Surface pressure**

Fig. 5 Rudder leading-edge surface values.

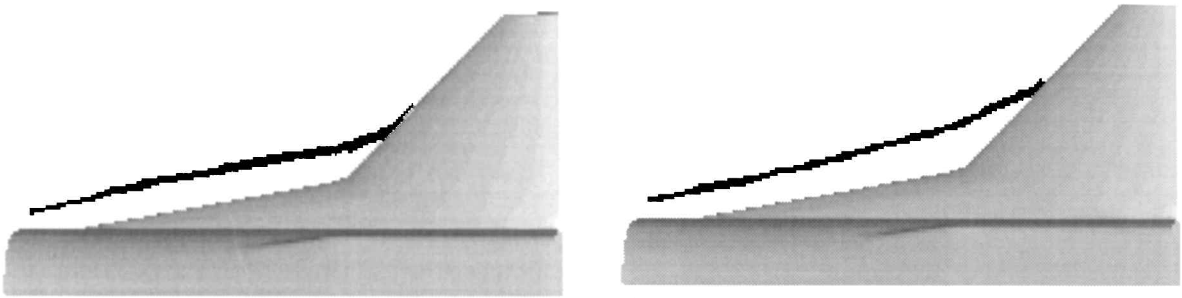

a) 152 s, *M* = 7.865 **d) 324 s, *M* = 6.94**

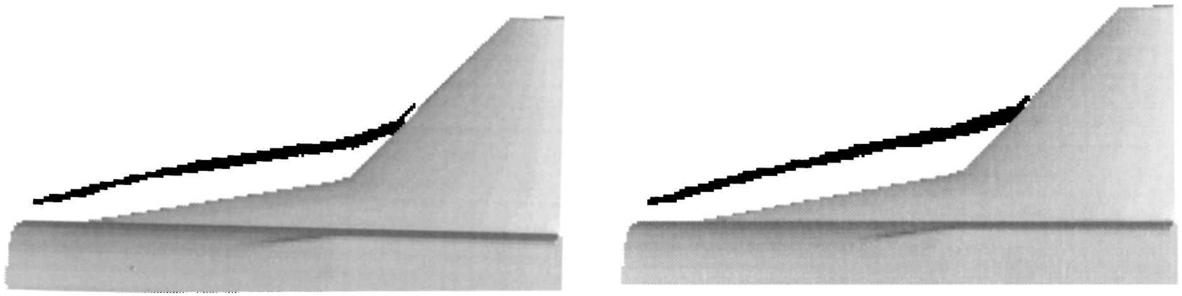

b) 221 s, *M* = 8.81 **e) 358 s, *M* = 6.3**

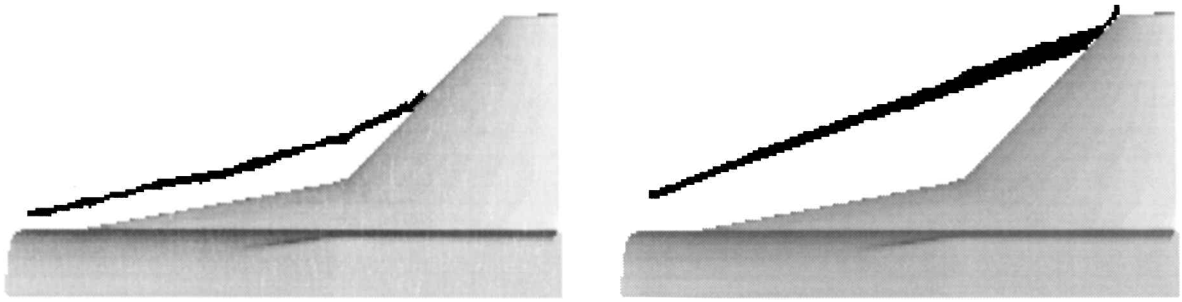

c) 294 s, *M* = 7.63 **f) 600 s, *M* = 4.44**

Fig. 6 Bow-shock wave impingement on wing leading edge.

in height and is shielded from the bow-shock wave by the comparatively lengthy fuselage at a positive angle of attack. If there are any instances in the flight path where the X-34 vehicle experienced a negative angle of attack, there is a chance the bow-shock wave might impinge on the rudder leading edge.

Grid Sensitivity

Any proper computational analysis must include an assessment of the grid dependence of the solutions. A grid sensitivity analysis was performed using the nosecap and along the wing/strake leading-edge grids. The analysis was performed at the 324-s trajectory point because this is where the peak heating occurred for the nosecap and wing/strake leading-edge calculations.

The $65 \times 65 \times 65$ nosecap grid used in the six computations presented earlier had an initial spacing off the body of 1.0*e*−6 m. Solutions were also generated using two other grids: The first was a $65 \times 65 \times 33$ grid with an initial normal spacing of 2.0*e*−6 m, and the second was a $65 \times 65 \times 129$ grid with an initial normal

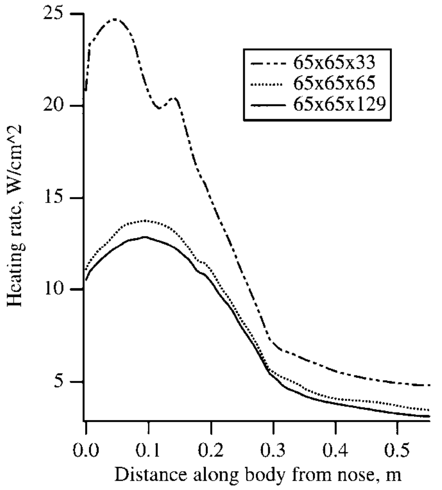

a) Windward centerline

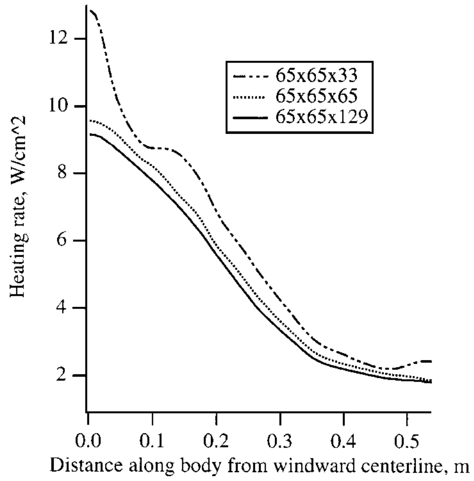

b) Circumferential plane, *s* = 0.23 m

Fig. 7 Grid sensitivity study, nosecap, 324-s trajectory point.

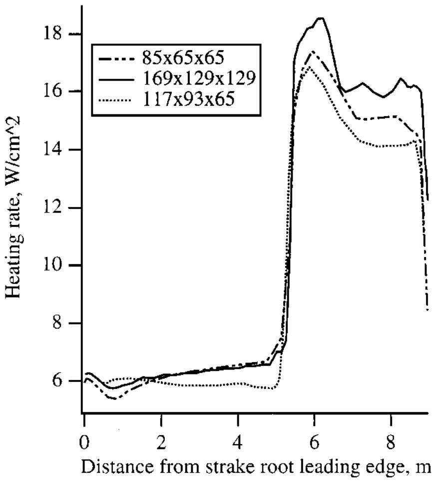

a) Wing/strake leading edge

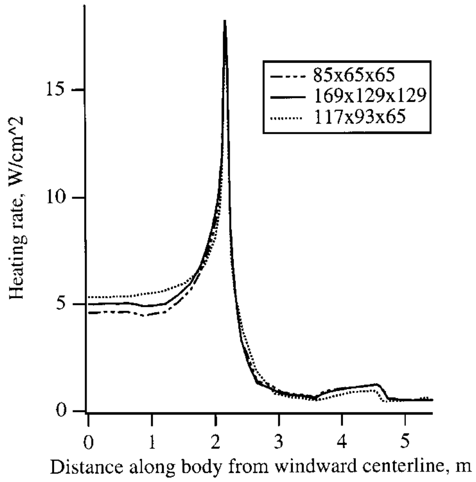

b) Circumferential plane, *s* = 5.95 m

Fig. 8 Grid sensitivity study, wing/strake region, 324-s trajectory point.

spacing of 0.5*e*−6 m. Results for the three nosecap grids are shown in Fig. 7. Heating rate profiles along the windward centerline are shown in Fig. 7a, and heating rate profiles along a circumferential plane 0.23 m from the nose are shown in Fig. 7b. The grid with 33 normal lines clearly does not have sufficient spatial resolution. The heating rate profile differs greatly from the nominal 65 × 65 × 65 grid. Increasing the point number in the normal direction from 65 to 129 points does not significantly change the solution. The maximum difference along the windward centerline is less than 5%. The nominal 65 × 65 × 65 grid provided sufficient spatial resolution to reduce the solution grid dependence to an acceptably low amount.

A similar study was performed on the wing/strake grid. The nominal 85 × 65 × 65 solution at the 324-s point was compared with a solution generated using a 169 × 129 × 129 grid that doubled the grid resolution in all three coordinate directions. The heating rate profiles along the wing/strake leading edge and along a circumferential plane at the wing/strake junction for these two grids are shown in Fig. 8. Also shown in these plots are solutions from the rudder grid, previously designated as grid 3. The rudder grid had far less resolution of the wing/strake leading edge than either of the wing/strake grids. The two wing/strake solutions are virtually identical along the strake leading edge. The rudder grid shows some discrepancies from the wing/strake solutions along the strake leading edge but is still reasonably close. The 169 × 129 × 129 grid shows a higher heating along the wing leading edge. The rudder grid, with the least spatial resolution along the wing leading edge, shows the heating level below the other two. The maximum difference between the wing/strake grids in the region of the bow-shock impingement is 7.1%. The circumferential profiles are virtually identical between all three solutions.

This study does not represent a comprehensive grid sensitivity study. Parametric studies varying the first normal grid spacing and shock-layer resolution would provide a more rigorous evaluation of the grid dependence of the preceding solutions. Further grid sensitivity studies were not performed due to the expense of doing such things over a complex, three-dimensional vehicle.

Concluding Remarks

Computations have been performed over the X-34 vehicle at six points along the X1004701 Mach 8.5 trajectory. The calculations focused on computing the surface heating rate and pressure on the nosecap, wing/strake leading edge, and rudder leading edge, surfaces that will be protected from the thermal environments experienced during flight by SIRCA tiles. The CFD solution was first validated against experimental data. The CFD solutions will provide anchor points from which a time history of the surface heating rate and pressure can be generated. This time history will be used by the tile designers to analyze the tile design. Solution run time and resource requirements for the CFD computations were a function of the grid size. A typical computation on the wing/strake grid required 40 Cray C-90 computer hours and 50 MW of run-time memory.

A qualitative assessment was performed on the location and effects of bow-shock wave impingement on the wing leading edge. The location of impingement was a function of freestream Mach number and vehicle angle of attack. There was no bow-shock wave impingement seen on the rudder leading edge. The grid dependence of the solutions was assessed.

Regarding the numerical uncertainties of the preceding CFD computations, the GASP flow solver, by the Space Shuttle computations[8] and other validation efforts, has shown itself to be reasonably accurate at predicting heat transfer in regions of compression and less accurate in regions of expansion. There is very little uncertainty with regard to the thermochemical model because the flow at all six trajectory points was essentially a perfect gas. Turbulent flow calculations always have more uncertainty because of uncertainties in the turbulence models. Therefore, the nosecap computations, generally speaking, had less uncertainty than the wing/strake and rudder leading-edge computations because of greater spatial resolution of the nosecap surface and the fact that the nosecap solutions were all laminar computations. The wing/strake leading edge is in a region of compression, but additional uncertainties arise because of a coarser spatial resolution of the wing/strake leading edge and the fact that five of the six computations were run turbulent. The rudder leading-edge computation has the most uncertainty because it is on the leeward side of the vehicle and five of the six solutions were run turbulent.

References

[1] Merski, N. R., "Global Aeroheating Wind-Tunnel Measurements Using Improved Two-Color Phosphor Thermography Method," *Journal of Spacecraft and Rockets*, Vol. 36, No. 2, 1999, pp. 160–170.

[2] Kleb, W. L., Wood, W. A., Gnoffo, P. A., and Alter, S. J., "Computational Aeroheating Predictions for X-34," *Journal of Spacecraft and Rockets*, Vol. 36, No. 2, 1999, pp. 179–188.

[3] Berry, S. A., Horvath, T. J., DiFulvio, M., Glass, C., and Merski, N. R., "X-34 Experimental Aeroheating at Mach 6 and 10," *Journal of Spacecraft and Rockets*, Vol. 36, No. 2, 1999, pp. 171–178.

[4] Wurster, K. E., Riley, C. J., and Zoby, E. V., "Engineering Aerothermal Analysis for X-34 Thermal Protection System Design," *Journal of Spacecraft and Rockets*, Vol. 36, No. 2, 1999, pp. 216–228.

[5] Steinbrenner, J. P., and Chawner, J. R., "The GRIDGEN Version 9 Multiple Block Grid Generation Software," MDA Engineering, Inc., Rept. 94-01, Arlington, TX, June 1994.

[6] Walters, R. W., Slack, D. C., Cinnella, P., Aplebaum, M., and Frost, C., "A User's Guide to GASP," Virginia Polytechnic Inst. and State Univ., Research Rept. on NASA Grants NAG-1-766 and NAG-1-1045, Blacksburg, VA, Nov. 1990.

[7] Gnoffo, P., Weilmuenster, K., and Alter, S., "Multiblock Analysis for Shuttle Orbiter Re-Entry Heating from Mach 24 to Mach 12," *Journal of Spacecraft and Rockets*, Vol. 31, No. 3, 1994, pp. 367–377.

[8] Olynick, D. R., and Tam, T., "Trajectory Based Validation of the Shuttle Heating Environment," AIAA Paper 96-1891, June 1996.

[9] Olynick, D. R., and Henline, W. D., "Numerical Benchmarks for Navier–Stokes Heating Calculations on Access to Space Vehicles," AIAA Paper 95-2078, June 1995.

[10] Henline, W. D., Palmer, G. E., Milos, F. S., Olynick, D. R., and Chen, Y.-K., "Aerothermodynamic Heating Analysis and Heatshield Design of an SSTO Rocket Vehicle for Access-to-Space," AIAA Paper 95-2079, June 1995.

[11] Palmer, G., Henline, W. D., Olynick, D. R., and Milos, F. S., "A Heating Analysis and Thermal Protection System Sizing of a Lifting Body Single-Stage-to-Orbit Vehicle," AIAA Paper 95-2080, June 1995.

[12] Park, C., "On Convergence of Computation of Chemically Reacting Flows," AIAA Paper 85-0247, Jan. 1985.

[13] Blottner, F. G., Johnson, M., and Ellis, M., "Chemically Reacting Viscous Flow Program for Multi-Component Gas Mixtures," Sandia Labs., SC-RR-70-754, Albuquerque, NM, Dec. 1971.

[14] Wilke, C. R., "A Viscous Equation for Gas Mixtures," *Journal of Computational Physics*, Vol. 18, No. 4, 1950, pp. 517–519.

[15] Vincenti, W. G., and Kruger, C. H., *Introduction to Physical Gas Dynamics*, Krieger, Malabar, FL, 1965, p. 21.

[16] Baldwin, B., and Lomax, H., "Thin Layer Approximation and Algebraic Model for Separated Turbulent Flows," AIAA Paper 78-0257, Jan. 1978.

[17] Tauber, M. E., "A Review of High-Speed Convective, Heat-Transfer Computation Methods," NASA TP-2914, Sept. 1989.

[18] Fay, J. A., and Ridell, F. R., "Theory of Stagnation Point Heat Transfer in Dissociated Air," *Journal of the Aeronautical Sciences*, Vol. 25, No. 2, 1958, pp. 73–85.

[19] Anderson, J. D., *Hypersonic and High Temperature Gasdynamics*, McGraw–Hill, New York, 1989, p. 280.

[20] Bowcutt, K. G., Anderson, J. D., and Capriotti, D., "Viscous Optimized Hypersonic Waveriders," AIAA Paper 81-0272, Jan. 1987.

T. C. Lin
Associate Editor